J. Fluid Mech. (2020), *vol.* 899, A7. © The Author(s), 2020.
Published by Cambridge University Press
doi:10.1017/jfm.2020.385

Air sheet contraction

Zhen Jian[1,‡], **Peng Deng**[1,‡] **and Marie-Jean Thoraval**[1,†]

[1]State Key Laboratory for Strength and Vibration of Mechanical Structures, International Center for Applied Mechanics, School of Aerospace, Xi'an Jiaotong University, Xi'an 710049, PR China

(Received 11 October 2019; revised 6 February 2020; accepted 11 May 2020)

A two-dimensional air sheet in a surrounding liquid contracts under surface tension. We investigate numerically and analytically this contraction dynamics for a range of Ohnesorge numbers Oh. In a similar way as for liquid films, three contraction regimes can be identified based on the Oh: vortex shedding, smooth contraction and viscous regime. For $Oh \leqslant 0.02$, the rim can even pinch-off due to the rim deformations caused by the vortex shedding. In contrast with a liquid film that continuously accelerates towards the Taylor–Culick velocity when the surrounding fluid can be neglected, the air film contraction velocity first rises to a maximum value U_{max} before decreasing due to the drag of the external fluid on the moving rim. This U_{max} follows a capillary-inertial scaling at low Oh and continuously shifts to a capillary-viscous scaling with increasing Oh. We demonstrate that the decreasing contraction velocity scales as $t^{-0.15}$, which is faster than the scaling $t^{-0.2}$ derived under the assumption of a constant drag coefficient. The transition between the capillary-inertial and capillary-viscous regimes can be characterised by the local time evolving Ohnesorge number Oh_δ based on the thickness of the rim. The oscillations of the rim appear at a critical local Weber number We_δ. Then they follow a well-defined oscillation frequency with a characteristic Strouhal number. Beyond a local Reynolds number larger than 200, the oscillations become more irregular with more complex vortex sheddings, eventually leading to the pinch-off of the rim.

Key words: drops and bubbles

1. Introduction

The breakup and contraction of an air sheet has important applications for a large range of interface-related processes in nature and industry, such as in the formation of bubbles at the surface of the sea (Wanninkhof *et al.* 2009; Czerski *et al.* 2011; Kiger & Duncan 2012; Deike, Melville & Popinet 2016), or the air entrapment in inkjet printing or coating technologies (de Gennes, Brochard-Wyart & Quéré 2004; Yarin 2006; Derby 2010; Josserand & Thoroddsen 2016). Such air films can be entrapped by the impact of a drop on a pool due to the air lubrication pressure (Hicks & Purvis 2011; Tran *et al.* 2013; Josserand, Ray & Zaleski 2016). At high

† Email address for correspondence: mjthoraval@xjtu.edu.cn
‡ These authors contributed equally to this work.

https://doi.org/10.1017/jfm.2020.385 Published online by Cambridge University Press

impact velocities the air is entrapped in an air disk (Thoroddsen, Etoh & Takehara 2003; Thoraval & Thoroddsen 2013; Jian *et al.* 2020). At low impact velocities, the air film can be stretched between the drop and the pool before contact, leading to the entrapment of a large number of microbubbles (Esmailizadeh & Mesler 1986; Sigler & Mesler 1990; Mills, Saylor & Testik 2012; Saylor & Bounds 2012; Thoroddsen *et al.* 2012; Beilharz *et al.* 2015). If the air sheet completely wraps the drop, it forms an antibubble, important for biological and medical applications (Dorbolo, Caps & Vandewalle 2003; Dorbolo *et al.* 2005; Vandewalle *et al.* 2009; Dorbolo *et al.* 2010; Scheid *et al.* 2012; Zou *et al.* 2013; Scheid, Zawala & Dorbolo 2014; Beilharz *et al.* 2015; Sob'yanin 2015). While the contraction of a liquid film has been extensively investigated, only limited studies have focused on the contraction of an air film.

Taylor (1959) and Culick (1960) investigated independently the contraction of a thin liquid film and found a constant contraction velocity $U_{TC} = \sqrt{2\sigma/(\rho_l e)}$, where σ is the surface tension, ρ_l the liquid density and e the uniform film thickness. They showed that this formula can be explained by a balance between surface tension force and inertia of a growing rim accumulating all the liquid displaced (de Gennes *et al.* 2004). The liquid accelerates towards the Taylor–Culick velocity independently of the liquid viscosity (Pandit & Davidson 1990). The liquid viscosity, however, influences the time to reach this asymptotic value, where half of the initial surface energy is dissipated by viscous effect and the other half is converted to kinetic energy of the liquid sheet (Sünderhauf, Raszillier & Durst 2002). For very viscous films, the contraction velocity increases exponentially, with a characteristic rising time $\tau_\mu = \mu_l e/\sigma$, where μ_l is the liquid viscosity (Debrégeas, Martin & Brochard-Wyart 1995; Debrégeas, de Gennes & Brochard-Wyart 1998). The contraction of two-dimensional viscous liquid films can be classified into three regimes, depending on the Ohnesorge number and the Reynolds number based on the longitudinal extent of the film (Brenner & Gueyffier 1999; Savva & Bush 2009). Reyssat & Quéré (2006) found that the contraction of a fluid film in a viscous liquid is limited by the friction from the surrounding liquid, leading to the velocity scaling as the capillary-viscous velocity $U_\mu = \sigma/\mu_l$ with a logarithmic correction decreasing the velocity during the contraction. Chebil *et al.* (2018) then investigated the finite-size effects on the retraction dynamics of a thin polymer film embedded in another viscous liquid between solid surfaces.

A similar contraction mechanism as for a liquid film is also observed for an air film contracting in a liquid, with the displaced air accumulating into a rim. However, in this case the surface tension force pulling on the rim is balanced by the resistance of the surrounding liquid instead of the inertia of the rim. The contraction dynamics of this air film was first studied by Oguz & Prosperetti (1989) with inviscid boundary integral simulations. They found that the contraction velocity first increases rapidly up to a maximum velocity, scaling with the capillary-inertial velocity $U_\rho = \sqrt{\sigma/(\rho_l e)}$, and then decreases. This velocity was then successfully applied to model the contraction velocity of the air disk entrapped below a drop impacting on a pool, with an exponential decay explained by the increasing thickness of the film (Thoroddsen *et al.* 2003; Thoraval & Thoroddsen 2013). Thoroddsen *et al.* (2005) later demonstrated that the same contraction dynamics is also observed for the air disk entrapped below a drop impacting on a solid surface. The rupture velocity of the air films produced in the Mesler regime follows this capillary-inertial velocity scaling for lower viscosity liquids (Thoroddsen *et al.* 2012; Beilharz *et al.* 2015). For higher viscosity fluids, a viscous-capillary scaling U_μ would be expected (Eggers, Lister & Stone 1999; Thoroddsen *et al.* 2005; Reyssat & Quéré 2006; Chebil *et al.* 2018). However, much higher contraction velocities have been observed

https://doi.org/10.1017/jfm.2020.385 Published online by Cambridge University Press

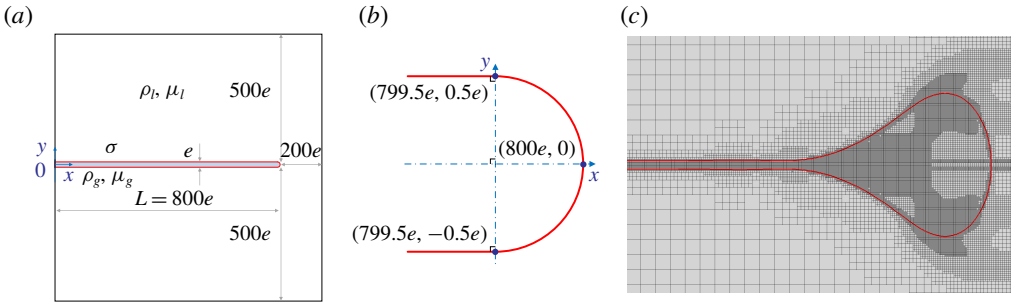


FIGURE 1. (*a*) Sketch of the computing domain. A long air sheet of thickness e and initial length $L = 800e$ with a half-circle cap is extending horizontally at the centre of a square computing domain of liquid of size $1000e$. The sheet is connected to the left-hand boundary of the domain and has a free end $200e$ away from the right-hand boundary. The sheet thickness is not represented to scale for clarity. (*b*) Initial profile of the tip of the sheet. Two parallel lines are tangent lines to the half-circle at the connection point. (*c*) Snapshot of the adaptive mesh refinement in the area of the rim of the sheet for $Oh = 0.3$ at $t^* = 500$. The red curve represents the interface.

experimentally (Thoroddsen *et al.* 2012; Langley & Thoroddsen 2019), suggesting that three-dimensional effects significantly affect the contraction dynamics in the viscous regime. Experiments on the rupture of antibubbles have shown that the rupture velocity of the air film decreases in time (Dorbolo *et al.* 2003). Zou *et al.* (2013) observed a nearly constant contraction velocity of the antibubble air film and proposed a potential flow model to explain this velocity. Their model can be understood as a direct equivalent of the Taylor–Culick velocity for the liquid film, with the inertia limiting the motion located in the added mass of the surrounding liquid rather than the rim. Sob'yanin (2015) pointed out that the potential assumption of Zou *et al.* (2013) is not valid for the bursting of an antibubble, because of the high local Reynolds number at the edge of the air sheet. He derived an analytical solution of the contraction velocity assuming that the contraction dynamics is controlled by a balance between surface tension force and the hydrodynamic drag force.

In this paper, we investigate the ideal configuration of a two-dimensional long flat air sheet contracting in a surrounding liquid by solving the two-phase Navier–Stokes equations. We systematically vary the Ohnesorge number to explore the different contraction dynamics. Previous studies have demonstrated that this two-dimensional (2-D) approach is relevant to capture some of the air film contraction dynamics (Thoroddsen *et al.* 2003; Reyssat & Quéré 2006; Thoraval & Thoroddsen 2013; Sob'yanin 2015). However, a complete understanding of this phenomenon will require three-dimensional (3-D) simulations and modelling to capture the instabilities and eventual bubble sheddings observed experimentally by Thoroddsen *et al.* (2003, 2012), which is left to further studies.

2. Problem and method

We consider a two-dimensional planar air sheet of uniform thickness e and initial length $L = 800e$ in a square computing domain of size $1000e$ (figure 1). The sheet is set horizontally at an equal distance between the top and bottom boundaries. The air and the surrounding liquid are taken as incompressible. A symmetric boundary

https://doi.org/10.1017/jfm.2020.385 Published online by Cambridge University Press

condition is imposed on the four sides of the domain, thus conserving the volume of air and liquid in the domain. The left-hand side of the air sheet reaches the side of the domain with a stable 90° contact angle. The other side initially ends at $x = 800e$ with a half-circular cap of diameter equal to the thickness e, $200e$ away from the right-hand boundary. The gas with density ρ_g and viscosity μ_g is surrounded by a liquid of density ρ_l and viscosity μ_l, with surface tension σ. The air sheet contracts from rest under surface tension at a velocity U and accumulates the displaced air into a rim. We verified that the initial shape of the rim and the size of the domain do not influence the contraction dynamics (see supplementary material, available at https://doi.org/10.1017/jfm.2020.385).

The dynamics are then characterised by the density ratio $\alpha = \rho_g/\rho_l$, the viscosity ratio $\beta = \mu_g/\mu_l$ and the Ohnesorge number Oh that compares the viscous, capillary and inertial effects

$$Oh = \frac{\mu_l}{\sqrt{\rho_l \sigma e}}. \tag{2.1}$$

The density and viscosity ratios are fixed to $\alpha = 1.23 \times 10^{-3}$ and $\beta = 0.02$, and we vary systematically the Ohnesorge number Oh. The simulations parameters are chosen based on the properties of an air film contracting in water. For $Oh = 0.1$, this would correspond to $e = 1.1$ μm, which is consistent with the typical thickness of an air disk entrapped below an impacting drop (Thoroddsen *et al.* 2003). Changing the Oh would be equivalent physically to changing the film thickness e.

We solve the incompressible two-phase Navier–Stokes equations

$$\rho \frac{D\boldsymbol{u}}{Dt} = -\boldsymbol{\nabla} p + \mu \Delta \boldsymbol{u} + \sigma \kappa \delta_s \boldsymbol{n}, \tag{2.2}$$

$$\boldsymbol{\nabla} \cdot \boldsymbol{u} = 0, \tag{2.3}$$

where D/Dt denotes the material derivative, p and $\boldsymbol{u}$ are the pressure and velocity, κ is the curvature of the interface, δ_s is a delta function to apply the surface tension at interface and $\boldsymbol{n}$ is the normal vector to the interface. The density ρ and viscosity μ take constant values in each phase.

The Navier–Stokes equations are solved in dimensionless form by the open source code Basilisk (Popinet 2019). We define the capillary-inertial velocity as $U_\rho = \sqrt{\sigma/(\rho_l e)}$ and the capillary time as $\tau_\rho = \sqrt{\rho_l e^3/\sigma}$. We then rescale the density, length, time, velocity and pressure by ρ_l, e, τ_ρ, U_ρ and σ/e, respectively. The non-dimensional equations can be written as

$$\rho^* \frac{D\boldsymbol{u}^*}{Dt^*} = -\boldsymbol{\nabla}^* p^* + Oh \mu^* \Delta \boldsymbol{u}^* + \kappa^* \delta_s^* \boldsymbol{n}, \tag{2.4}$$

using an asterisk for dimensionless variables. The density ρ^* and viscosity μ^* now take the value one in the liquid phase and α and β in the gas phase.

Basilisk uses a finite-volume method on an adaptive tree-structured (quad tree in two dimensions) mesh and the interface is tracked by a volume of fluid (VOF) method. Two criteria for mesh refinement were applied in our simulations based on the VOF tracer and the u, v components of the velocity. Figure 1(*c*) shows an example of the adaptive mesh refinement in the rim area, where the interface and regions of high vorticity are highly refined. The maximum level of refinement is characterised by the refinement level n corresponding to a minimum cell size of $1/2^n$ times the size of the domain. The mesh independence was verified and $n = 13$ was chosen in this study to guarantee at least eight meshes inside the air sheet thickness e, namely $2^n e/L \geqslant 8$ (see supplementary material). The simulation results were saved every $\Delta t^* = 0.1$.

https://doi.org/10.1017/jfm.2020.385 Published online by Cambridge University Press

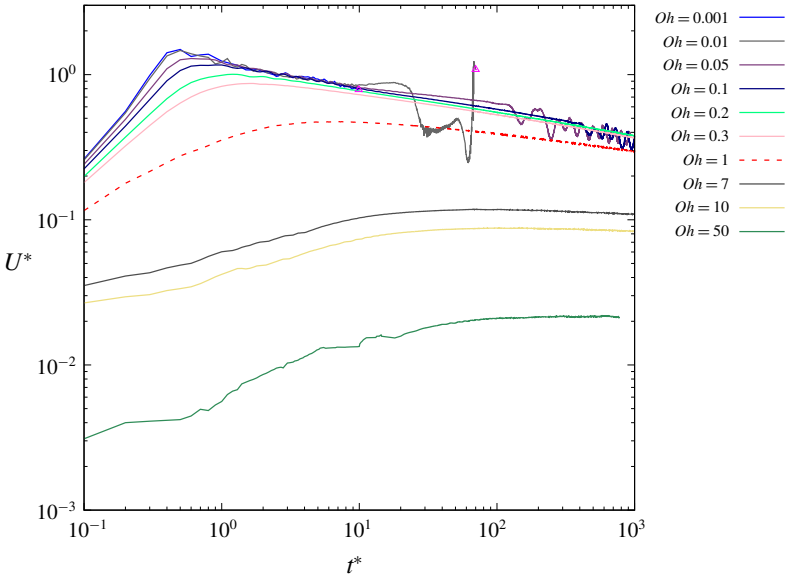


FIGURE 2. Contraction velocity of the rim $U^* = U/U_\rho$ versus time $t^* = t/\tau_\rho$ for different Ohnesorge numbers Oh in log–log scale. The data after pinch-off are not plotted, and the pinch-off time is indicated by an empty triangle at $t^* = 10.0$ for $Oh = 0.001$ and $t^* = 72.5$ for $Oh = 0.01$. A dashed line is used for $Oh = 1$ to identify it more clearly (see supplementary material for the figure including the full range of Oh).

3. Dynamics of the air sheet contraction

As the sheet starts contracting from rest under surface tension, the edge is accelerated and accumulates the gas into a rim (figure 1). The contraction velocity U^* increases to a maximum velocity U^*_{max} before decreasing (figure 2), in a similar way as previously reported by Oguz & Prosperetti (1989) and Sob'yanin (2015). The contraction velocity increases more rapidly and to a higher U^*_{max} for lower Oh. Some oscillations of the rim can be observed for $Oh \leqslant 0.1$ during the decreasing contraction velocity phase.

3.1. *Maximum contraction velocity*

As Oh tends to zero, the maximum contraction velocity converges to an asymptotic value $U^*_{max} = U_{max}/U_\rho \simeq 1.5$ at $t^*_{U_{max}} = t_{U_{max}}/\tau_\rho = 0.5$ before decreasing (figure 3). This scaling is characteristic of a capillary-inertial dominated dynamics. However, the maximum contraction velocity obtained here is larger than the Taylor–Culick velocity $U^*_{TC} = \sqrt{2}$ that would be obtained for a liquid film. Our results are consistent with the inviscid simulations of Oguz & Prosperetti (1989) focused on the initial contraction dynamics. They observed a maximum contraction velocity of approximately $U^*_{max-2D} \simeq 1.4$ for the two-dimensional simulations, larger than $U^*_{max-A} \simeq 1.2$ in the axisymmetric case. They even observed some oscillations of the contraction velocity during the acceleration phase, suggesting that the oscillations could appear even earlier in the inviscid limit. The antibubble rupture experiments of Dorbolo *et al.* (2003) and Zou *et al.* (2013) have a typical Ohnesorge number $Oh \simeq 0.1$, which is still in this capillary-inertial regime.

https://doi.org/10.1017/jfm.2020.385 Published online by Cambridge University Press

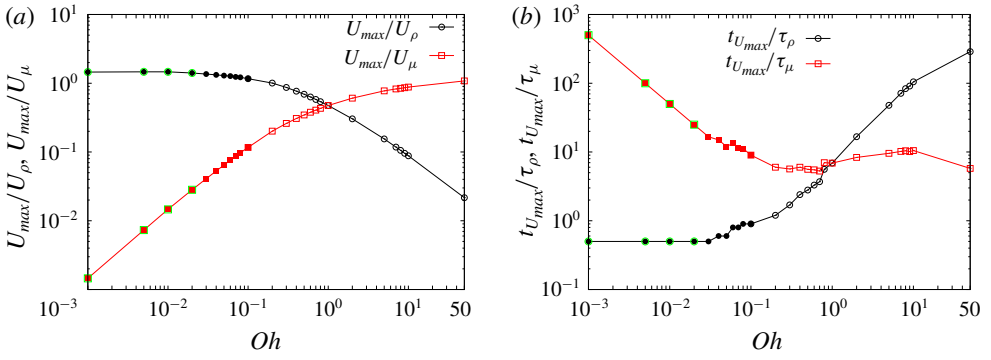


FIGURE 3. (*a*) Maximum contraction velocity of the rim U_{max} rescaled by the capillary-inertial velocity $U_\rho = \sqrt{\sigma/(\rho_l e)}$ and by the capillary-viscous velocity $U_\mu = \sigma/\mu_l$ as a function of the Ohnesorge number Oh in log–log scale. (*b*) Time to reach the maximum velocity $t_{U_{max}}$ rescaled by the capillary-inertial time $\tau_\rho = \sqrt{\rho_l e^3/\sigma}$ and by the capillary-viscous time $\tau_\mu = \mu_l e/\sigma$, respectively, as a function of the Ohnesorge number Oh in log–log scale. Solid symbols denote the cases for which the rim oscillates and solid symbols with green edges represent the cases with pinch-off. The dimensionless values used in the text are $U^*_{max} = U_{max}/U_\rho$ and $t^*_{U_{max}} = t_{U_{max}}/\tau_\rho$.

As the Oh number increases, the viscous dissipation decreases the maximum contraction velocity $U^*_{max} = U_{max}/U_\rho$, and the time to reach this maximum $t^*_{U_{max}} = t_{U_{max}}/\tau_\rho$ increases towards infinity. If we rescale them by the capillary-viscous scales $U_\mu = \sigma/\mu_l$ and $\tau_\mu = \mu_l e/\sigma$, the maximum contraction velocity U_{max}/U_μ converges towards an asymptotic value larger than one in a finite time $t_{U_{max}}/\tau_\mu$ (figure 3), in a consistent way with the relations

$$\frac{U_{max}}{U_\mu} = Oh\,\frac{U_{max}}{U_\rho} = Oh\,U^*_{max}, \tag{3.1}$$

$$\frac{t_{U_{max}}}{\tau_\mu} = \frac{1}{Oh}\,\frac{t_{U_{max}}}{\tau_\rho} = \frac{1}{Oh}\,t^*_{U_{max}}. \tag{3.2}$$

This capillary-viscous scaling is similar to what was observed by Eggers *et al.* (1999) and Reyssat & Quéré (2006) for the contraction of an air film in a viscous liquid, or by Reyssat & Quéré (2006) and Chebil *et al.* (2018) for the contraction of a liquid film in a viscous environment.

A similar trend to our figure 3(*a*) was also observed in Song & Tryggvason (1999) for the contraction of a liquid film. However, they underestimated the asymptotic contraction velocity due to a limited initial length of the film in their simulations (Sünderhauf *et al.* 2002).

3.2. *Three contraction regimes*

Three contraction dynamics regimes can be identified based on the Ohnesorge number Oh, in a similar way as for the contraction of a liquid film (Brenner & Gueyffier 1999; Savva & Bush 2009): vortex shedding regime, smooth contraction regime and viscous regime (figure 4).

For $Oh \leqslant 0.1$, some oscillations of the contraction velocity can be observed (figure 2). We formally define such oscillations when the y-coordinate of the

https://doi.org/10.1017/jfm.2020.385 Published online by Cambridge University Press

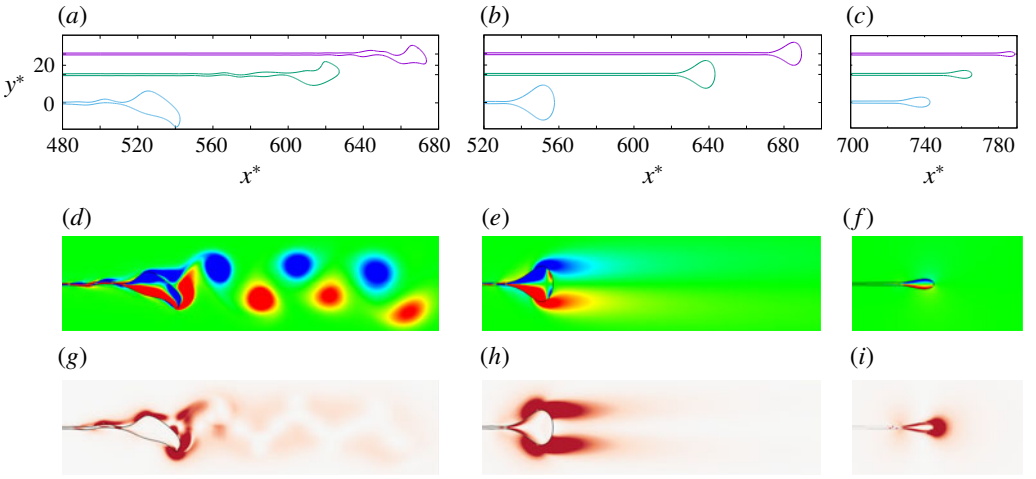


FIGURE 4. Three air film contraction regimes: (*a*,*d*,*g*, $Oh = 0.05$) vortex-shedding regime; (*b*,*e*,*h*, $Oh = 0.3$) smooth-contraction; and (*c*,*f*,*i*, $Oh = 7$) viscous regime. Panels (*a–c*) show the interface profile at $t^* = 200, 300, 500$ from top to bottom, with equal unit length along $x^* = x/e$ and $y^* = y/e$ axis, with $t^* = t/\tau_\rho$. Panels (*d–f*) and panels (*g–i*) show snapshots of vorticity contour and viscous dissipation at $t^* = 500$, respectively. The viscous dissipation rate is shown with a red shading in panels (*g–i*). See corresponding supplementary movies 1–3.

x-maximum point of the air sheet is larger than half of the initial sheet thickness ($|y^*_{x_{max}}| > 0.5$). These oscillations are characteristic of the deformations of the rim due to the shedding of vortices of alternating sign (figure 4*a*,*d*,*g*). This vorticity shedding is reminiscent of the von Kármán vortex street observed during the impact of a drop on a pool at high impact velocities (Thoraval *et al.* 2012; Castrejón-Pita, Castrejón-Pita & Hutchings 2012; Thoraval *et al.* 2013). Capillary waves propagate from the rim to the bulk of the sheet, in a similar way as observed for the contraction of a liquid sheet at low *Oh* numbers (Brenner & Gueyffier 1999; Song & Tryggvason 1999; Savva & Bush 2009; Gordillo *et al.* 2011). However, they do not remain symmetric across the centre of the sheet as for the liquid film, due to the vorticity shedding. The oscillations start earlier for smaller *Oh* (figure 2). For low enough *Oh* ($Oh \leqslant 0.02$), the oscillations can even induce the pinch-off of the rim (figure 5). The time of the first pinch-off decreases with decreasing *Oh*, at $t^* = 862.5, 72.5, 13.0, 10.0$ for $Oh = 0.02, 0.01, 0.005, 0.001$, respectively. The number of pinch-off events increases as the *Oh* decreases, with only one pinch-off observed for $Oh = 0.02$, and several pinch-offs for $Oh = 0.01, 0.005, 0.001$. For the lowest *Oh* numbers, the vorticity shedding becomes more irregular due to these pinch-off events (figure 5*c–e*). The rim oscillations are further analysed in § 4.4.

For larger *Oh* ($0.1 < Oh \leqslant 1$), the contraction of the film enters the smooth contraction regime (figure 4*b*,*e*,*h*). The oscillations and capillary waves are damped by viscosity. The rim is more stable and rounded, with a pair of counter-rotating symmetric vortices attached to it without separation.

For even larger *Oh* ($Oh \gg 1$), the viscous effects are more pronounced, producing a more elongated rim in the longitudinal axis (figure 4*c*,*f*,*i*). Only limited vorticity is produced around the rim, with the rim slowly accelerating towards its maximum velocity. The shape of the rim is further characterised in § 4.1.

https://doi.org/10.1017/jfm.2020.385 Published online by Cambridge University Press

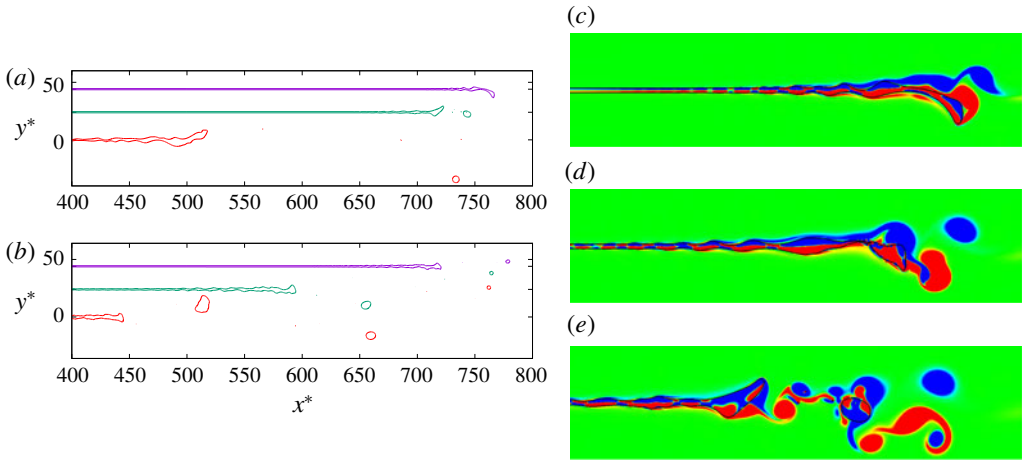


FIGURE 5. (*a*,*b*) Interface profiles of pinch-off: (*a*) $Oh = 0.01$ at $t^* = 50, 100, 500$ from top to bottom; (*b*) $Oh = 0.001$ at $t^* = 100, 300, 500$ from top to bottom. The interface profiles are plotted with equal unit length along axis x^* and y^*. The vertical position of the interface profile at $t^* = 500$ corresponds to the vertical axis, while the other two profiles are translated up for clarity. (*c–e*) Snapshots of vorticity contour in the rim area for $Oh =$ 0.01 at $t^* =$ (*c*) 50, (*d*) 72.5 and (*e*) 100, where pinch-off occurs at $t^* = 72.5$ and the black curve represents the interface. Here, $x^* = x/e$, $y^* = y/e$ and $t^* = t/\tau_\rho$. See corresponding supplementary movie 4.

3.3. *Asymptotic contraction velocity*

For all Oh numbers, the rim velocity decreases after reaching the maximum contraction velocity. This decrease was attributed to a competition between surface tension force and a hydrodynamic drag force by Sob'yanin (2015) for the rupture of an antibubble. For low Oh in our simulations, the decrease seems to follow a $U \sim t^{-0.15}$ power law (figure 6*a*).

We can formulate a similar theory for the contraction of a two-dimensional air sheet as for the spherical geometry considered by Sob'yanin (2015). The surface tension force pulls on the rim from both the top and bottom interfaces (figure 7), leading to a total force on the rim F_σ (de Gennes *et al.* 2004),

$$F_\sigma = 2\sigma. \tag{3.3}$$

It is balanced by the hydrodynamic drag force F_d on the rim of thickness δ, which can be expressed as

$$F_d = \tfrac{1}{2}\rho_l U^2 C_d \delta. \tag{3.4}$$

The balance between the surface tension force F_σ and the hydrodynamic drag force F_d gives

$$2\sigma = \tfrac{1}{2}\rho_l U^2 C_d \delta, \tag{3.5}$$

leading to

$$U = \sqrt{\frac{4\sigma}{\rho_l C_d \delta}}. \tag{3.6}$$

https://doi.org/10.1017/jfm.2020.385 Published online by Cambridge University Press

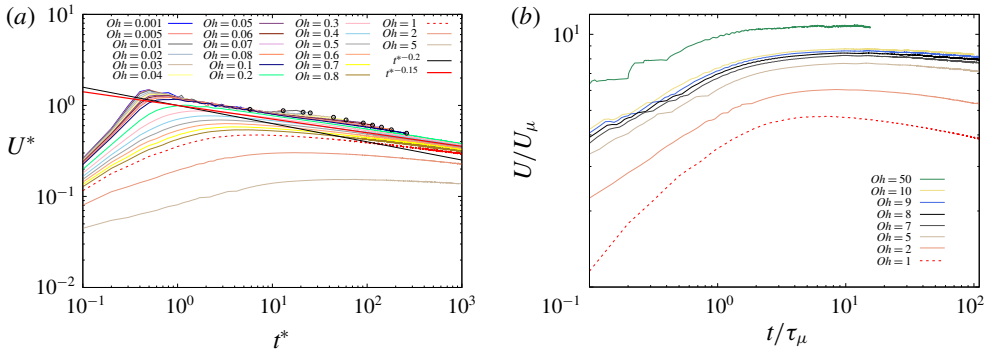


FIGURE 6. Contraction velocity of the rim versus time in log–log scale for (*a*) $Oh \leqslant 5$ with comparison to the scaling law $U^* = t^{*-0.2}$ (black solid line) and $U^* = t^{*-0.15}$ (red solid line). The oscillations observed for $Oh \leqslant 0.1$ in figure 2 are not plotted. The starting time of the oscillations is formally defined as the time when the y-coordinate of the x-maximum point of the air sheet first overcomes the height of the sheet ($|y_{x_{max}}| > 0.5e$), and indicated by an empty circle. A dashed line is used for $Oh = 1$ for clarity. Here, $U^* = U/U_\rho$, $t^* = t/\tau_\rho$. (*b*) $Oh \gg 1$: the velocity is rescaled by the capillary-viscous velocity $U_\mu = \sigma/\mu_l$ and time by the capillary-viscous time $\tau_\mu = \mu_l e/\sigma$. Here, $Oh = 1$, 2, 5 are included in both panels to capture the transition between the regimes.

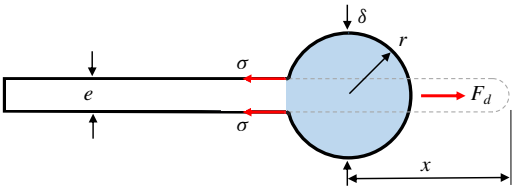


FIGURE 7. Sketch of force balance and mass conservation. The grey dashed line is the initial position of the air sheet and the blue area shows the accumulated mass at a later time t. Here, e is the initial thickness of the air sheet, δ is the thickness of the rim, r is the radius of the rim assuming a circular shape, x is the contraction distance, σ is the surface tension force on the top and bottom interfaces of the air sheet and F_d is the hydrodynamic drag force.

The contraction velocity of an air sheet therefore also follows a similar form as the Taylor–Culick velocity for the liquid film, but with a different length scale $C_d\delta/2$ characteristic of the rim size rather than the film thickness.

If we assume that the rim is circular with radius r, δ can be replaced by $2r$ in (3.6), leading to

$$U = \sqrt{\frac{2\sigma}{\rho_l C_d r}}. \tag{3.7}$$

A second equation can be obtained from the conservation of mass of the air displaced. When the air sheet contracts to a distance x from the initial position, a volume of air xe is then accumulated in the rim (figure 7),

$$\pi r^2 = xe. \tag{3.8}$$

https://doi.org/10.1017/jfm.2020.385 Published online by Cambridge University Press

By substituting (3.8) into (3.7), we obtain the geometrical dependence of the contraction velocity U,

$$U = \left(\frac{\pi}{e}\right)^{0.25} \left(\frac{2\sigma}{\rho_l C_d}\right)^{0.5} x^{-0.25}. \tag{3.9}$$

Sob'yanin (2015) modelled the dynamics of the rim in the case of an antibubble rupture in the same way as a circular solid cylinder with a no-slip boundary condition and a constant drag coefficient C_d. If we also assume a constant C_d, equation (3.9) can be solved analytically,

$$U = \left(\frac{4\pi}{5e}\right)^{0.2} \left(\frac{2\sigma}{\rho_l C_d}\right)^{0.4} t^{-0.2}. \tag{3.10}$$

In dimensionless form this is

$$U^* = Ct^{*-0.2}, \quad \text{with } C = \left(\tfrac{16}{5}\pi\right)^{0.2} C_d^{-0.4}. \tag{3.11}$$

This theory therefore predicts a power law decay of the contraction velocity in time. It is added as a black solid line in figure 6(*a*) with $C = 1$, corresponding to $C_d = 3.17$. Although the trend is similar, we observe that the film contraction is consistently faster than this scaling, following a scaling closer to the red solid line in figure 6(*a*)

$$U^* \sim t^{*-0.15}. \tag{3.12}$$

This slightly different scaling of the contraction velocity decay could be due to several reasons.

(i) The theory of a constant drag coefficient established for solid cylinders with a no-slip surface does not apply here for an air cylinder. The boundary condition is closer to a free-slip boundary condition, due to the low density of the gas in the film. As argued by Legendre, Lauga & Magnaudet (2009), the drag coefficient is reduced significantly by applying a shear-free boundary condition on a solid cylinder. A drag coefficient for bubbles can still be defined. However, experiments on the rising of a single bubble in water demonstrated that the drag coefficient C_d shows fluctuation and C_d is not only related to the Reynolds number but also to the geometry of the bubble (Tomiyama *et al.* 1998; Yan *et al.* 2017). The variations of the drag coefficient could thus affect the scaling of the contraction velocity (see § 4.1).

(ii) We have assumed that the rim is circular to derive this power law decay. This is in sharp contrast with the Taylor–Culick velocity established for the contraction of a liquid film without any assumption on the shape of the rim. The air cylinder is not exactly a circle, with a shape evolving in time and with the *Oh* number (figure 4). The shape of the rim could also play a role in the scaling observed (see § 4.1).

(iii) Finally, we have neglected the added mass of the surrounding liquid, characteristic of the accelerations of the rim. This will be important in the acceleration phase and in the oscillations regime, but can probably be neglected in the asymptotic regime as discussed by Sob'yanin (2015).

https://doi.org/10.1017/jfm.2020.385 Published online by Cambridge University Press

In the viscous regime at large Oh, we expect the contraction velocity to reach the capillary-viscous velocity $U_\mu = \sigma/\mu_l$ over the time scale $\tau_\mu = \mu_l e/\sigma$ and then decay slowly following a logarithmic correction (Reyssat & Quéré 2006). We have confirmed already these scalings for the maximum contraction velocity in figure 3. We focus here on the time evolution of the velocity after reaching the maximum (figure 6*b*). However, these high viscosity simulations require a longer computational time. The smaller decay regime observed in our simulations is not sufficient to obtain conclusive results about the asymptotic regime beyond the scaling velocity. Even if a 2-D asymptotic theory can be established, the two-dimensional assumption made in our simulations may not be physical, due to the three-dimensional destabilisation of the rim (Thoroddsen *et al.* 2012). Further studies will therefore be needed to answer these questions.

3.4. *Energy budget*

The drag coefficient model of the air film contraction presented above suggests that viscosity plays a more important role for the contraction of an air sheet compared to a liquid sheet. This is also suggested by the viscous dissipation around the vorticity regions observed in figure 4. The system initially only has surface energy E_{s0}, converted to kinetic energy E_k and viscous dissipation E_μ during the contraction (figure 8*a–c*). The rate of transfer is slower at higher Oh, due to the lower contraction velocity. However, a larger part is dissipated by viscous effects as the Oh increases (figure 8*d*). This is in strong contrast to the contraction of a liquid sheet, for which the energy is equally distributed between the kinetic energy and viscous dissipation (Sünderhauf *et al.* 2002; Savva & Bush 2009). This behaviour is only observed at the lowest Oh for the contraction of an air film, with $E_\mu/E_k \approx 1$ at $Oh = 0.001$ (figure 8*d*). The fundamental difference between the contraction of an air film and a liquid film can therefore be explained by the stronger viscous dissipation effects for the air film.

4. Dynamics of the rim

The first part of the analysis of the air sheet contraction dynamics was based on a dimensional analysis with the sheet thickness e as the relevant length scale. It provided a constant global Ohnesorge number $Oh = \mu_l/\sqrt{\rho_l \sigma e}$ and constant velocity scales to characterise the dynamics of each simulation. However, the theoretical modelling of the contraction velocity derived in § 3.3 suggested that the contraction velocity of the rim is controlled by its thickness δ (see (3.6)). This implies that the contraction dynamics is better characterised by the time evolving local geometry of the rim rather than the thickness of the air sheet. This is also supported by the transitions to oscillations and pinch-off regimes of the rim triggered at earlier times for lower Ohnesorge numbers.

In this section, we therefore investigate the contraction dynamics of the air film considering the instantaneous geometry of the rim. We first analyse the rim geometry to verify the assumptions made for the modelling of the contraction velocity. We then focus on the triggering and dynamics of the rim oscillations. We discuss especially the relevance of the comparison with the flow around a solid cylinder, in terms of drag coefficient and transition to vortex shedding.

4.1. *Rim geometry*

The evolution of the rim geometry with time and Oh is shown in figure 9(*a*,*c*,*e*), by translating horizontally the interface profiles to superpose the end points of the film.

https://doi.org/10.1017/jfm.2020.385 Published online by Cambridge University Press

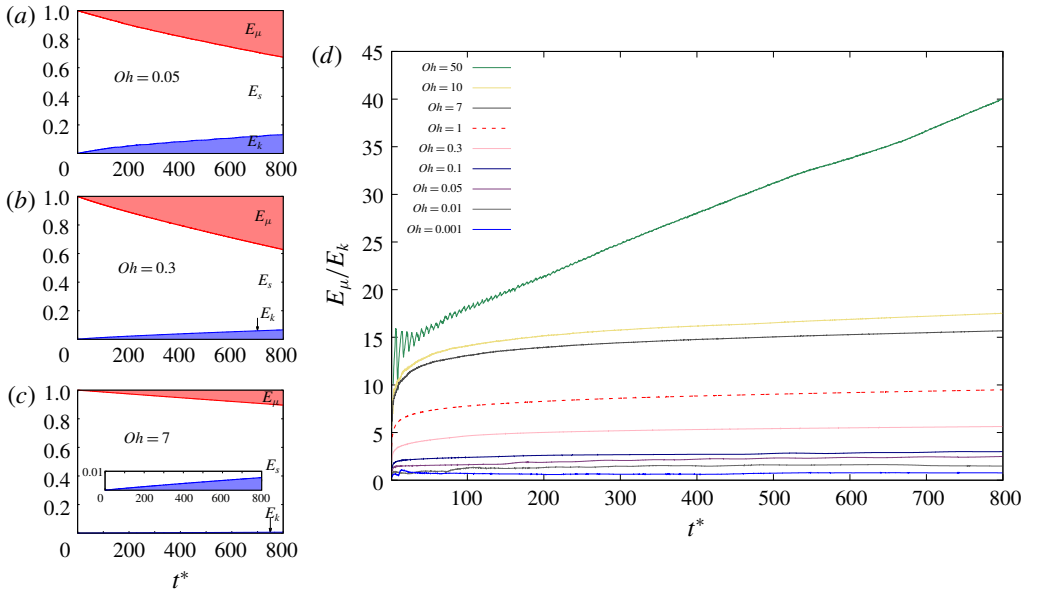


FIGURE 8. (*a–c*) Temporal evolution of energy budget, with surface energy E_s in white, kinetic energy E_k in blue and viscous dissipation E_μ in red, normalised by the initial surface energy E_{s0} for the three regimes: (*a*) vortex-shedding regime, $Oh = 0.05$, (*b*) smooth-contraction regime, $Oh = 0.3$ and (*c*) viscous regime, $Oh = 7$, corresponding to the three cases presented in figure 4. Inset in (*c*) is a zoom of the kinetic energy. (*d*) Ratio between viscous dissipation E_μ and kinetic energy E_k versus time t^*. A dashed line is used for $Oh = 1$ for clear view and $t^* = t/\tau_\rho$ (see supplementary material for the figure including the full range of Oh).

It confirms our modelling assumption that all the air displaced accumulates into a rim. The interface of the film beyond the rim is only disturbed at low Oh, first by capillary waves propagating from the rim, and then by asymmetric oscillations due to vortex shedding.

From the scaling law of the contraction velocity $U^* \sim t^{*-0.15}$ observed at lower Oh (3.12), the profiles of a circular rim would collapse together when rescaling both axis by $t^{*0.425}$. The rescaled profiles presented in figure 9(*b*,*d*,*f*) indeed nearly overlap into a single shape, except for the oscillations regimes. However, we still observe some significant deviations, characteristic of the shape evolution of the rim, becoming more elongated in the vertical direction over time. The constant drag coefficient theory would have predicted a collapse of the rim profiles when rescaling by a slightly different power law $t^{*0.4}$, from $U^* \sim t^{*-0.2}$ (3.11) as previously observed by Mirjalili, Chan & Mani (2018). A similar collapse is also observed for this rescaling as presented in figure S9 of the supplementary material, due to the small difference of power law, but with significantly larger deviations.

The deviations from a circular profile can be quantified by measuring the aspect ratio of the rim ξ, defined as its horizontal size divided by its thickness (figure 10). It can be formally defined by tracking the dynamics of three characteristic points of the rim (see inset of figure 10*b*): the top point, y-maximum point (x_t, y_t); the bottom point, y-minimum point (x_b, y_b); and the end point, x-maximum point $(x_{max}, y_{x_{max}})$. The aspect ratio of the rim ξ is then defined as $\xi = 2a/\delta$ with $a = x_{max} - 0.5(x_t + x_b)$ the

https://doi.org/10.1017/jfm.2020.385 Published online by Cambridge University Press

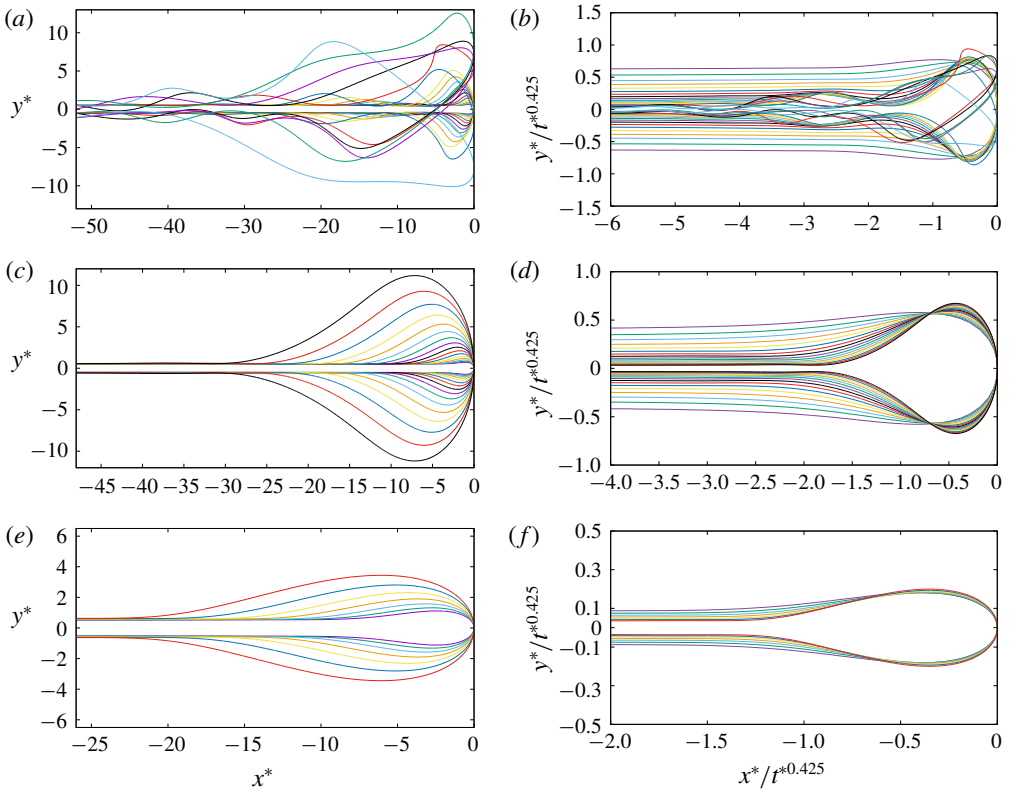


FIGURE 9. Evolution of the rim profiles in the three regimes presented in figure 4: (*a*,*b*, $Oh = 0.05$) vortex-shedding regime, (*c*,*d*, $Oh = 0.3$) smooth-contraction regime and (*e*,*f*, $Oh = 7$) viscous regime. On the left-hand side (*a*,*c*,*e*), the profiles are translated to the same end point. On the right-hand side (*b*,*d*,*f*) both axis of the profiles are also rescaled by $t^{*0.425}$. We show the first profile at the time of maximum contraction velocity $t_1^* = t_{U_{max}}^*$ to capture the stable regime of the contraction dynamics. Then the next time steps follow a logarithmic progression $t_{n+1}^* = 1.5t_n^*$ to capture the slow evolution of the rim up to $t^* = 1000$. The times of the first and last profiles are: $t_1^* = 0.6$, $t_{19}^* = 886.7$, at $Oh = 0.05$; $t_1^* = 1.7$, $t_{16}^* = 744.4$, at $Oh = 0.3$ and $t_1^* = 71.4$, $t_7^* = 813.3$, at $Oh = 7$. Here, $x^* = x/e$, $y^* = y/e$ and $t^* = t/\tau_\rho$ (see supplementary material for the comparison between the rescaled profile deduced from the scaling law of contraction velocity $t^{*-0.15}$ and $t^{*-0.2}$).

horizontal distance between the x-maximum point of the rim $(x_{max}, y_{x_{max}})$ and the centre of the rim $0.5(x_t + x_b)$, and $\delta = y_t - y_b$ the thickness of the rim.

For all Oh, the aspect ratio ξ starts from the value one, corresponding to the half-circle initial profile of the edge. During the acceleration phase, it first increases rapidly, becoming more elongated horizontally, before decreasing. For the cases without oscillation ($Oh > 0.1$), the aspect ratio then continues decreasing in time. This is consistent with the height of the rescaled rim increasing in time as observed in figure 9(*d*,*f*). As the Oh increases, the aspect ratio curves move higher, corresponding to the flattening of the rim in the viscous regime observed in figure 9(*e*). In contrast, at low Oh ($Oh \leqslant 0.1$) the decrease of the aspect ratio of the rim is much faster. After reaching a minimum value, corresponding to a maximal relative vertical extension, the aspect ratio ξ then increases in time until oscillations. The oscillations of the rim then

https://doi.org/10.1017/jfm.2020.385 Published online by Cambridge University Press

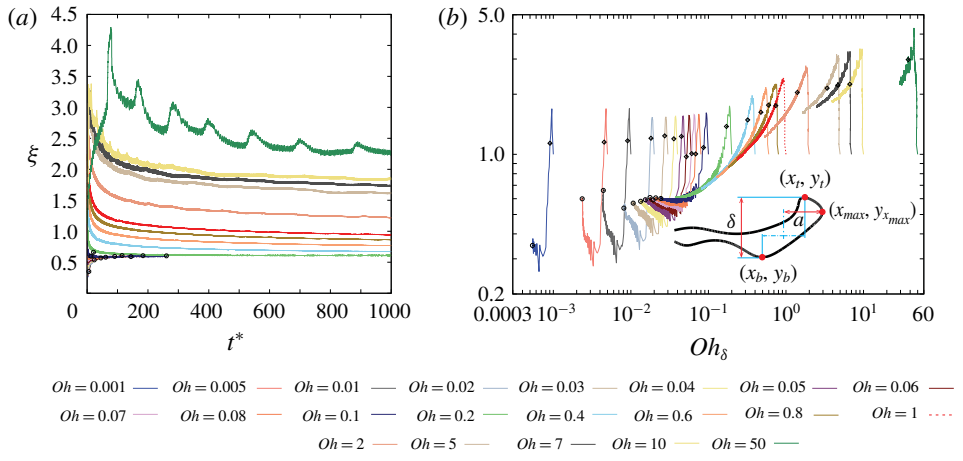


FIGURE 10. Aspect ratio of the rim ξ versus time t^* in linear scale (a), and versus the local Ohnesorge number $Oh_\delta = \mu_l/\sqrt{\rho_l \sigma \delta}$ in log–log scale (b). The aspect ratio ξ corresponding to the maximum contraction velocity is indicated by an empty diamond, the aspect ratio ξ corresponding to the starting time of the oscillations is indicated by an empty circle and the data after oscillation are not plotted for $Oh \leqslant 0.1$. Inset shows the definition of the aspect ratio $\xi = 2a/\delta$ and the rim profile is taken from $Oh = 0.05$ at $t^* = 175$. A dashed line is used for $Oh = 1$ for clarity. Here, $t^* = t/\tau_\rho$ (see supplementary material for the figure including the full range of Oh).

stretches it horizontally reaching values $\xi > 1$ (see figure 9(a,b) and supplementary material).

The variations of ξ with time and Oh can be understood from the local Ohnesorge number of the rim Oh_δ, defined as

$$Oh_\delta = \frac{\mu_l}{\sqrt{\rho_l \sigma \delta}}.$$

When plotted against Oh_δ in figure 10(b), all the aspect ratios follow a similar trend, from a vertically elongated rim at low Oh_δ to a rim horizontally elongated at large Oh_δ. The aspect ratio curves do not exactly collapse onto a single curve, suggesting that more parameters play a role in this correlation between the geometry and the local flow properties.

4.2. *Drag coefficient*

Based on this quantitative analysis of the rim geometry, we can discuss the validity of the modelling assumptions made in § 3.3. We can visualise the resistance of the flow to the motion of the rim by measuring the drag coefficient C_d, estimated as $C_d = 4\sigma/(\rho_l U^2 \delta)$ from (3.5) only assuming a negligible added mass effect. In figure 11, we show C_d as a function of the local Reynolds number Re_δ of the rim, defined as

$$Re_\delta = \frac{\rho_l U \delta}{\mu_l}.$$

If we ignore the acceleration phase, affected by the added mass effect, a clear trend emerges, very similar to the drag coefficient of a solid cylinder. At low Reynolds

https://doi.org/10.1017/jfm.2020.385 Published online by Cambridge University Press

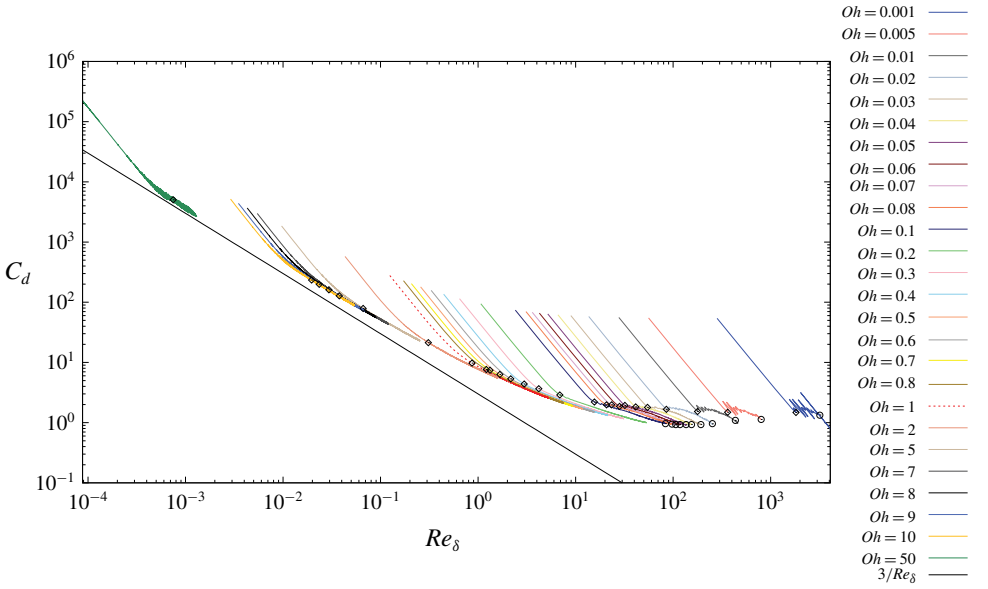


FIGURE 11. Drag coefficient C_d, calculated as $C_d = 4\sigma/(\rho_l U^2 \delta)$ following (3.5), versus the local Reynolds number Re_δ in log–log scale for different Ohnesorge numbers. The scaling $3/Re_\delta$ is plotted for comparison. The drag coefficient C_d corresponding to the maximum contraction velocity is indicated by empty diamonds, the drag coefficient C_d corresponding to the starting time of the oscillations is indicated by empty circles and the data after oscillation are not plotted for $Oh \leqslant 0.1$. A dashed line is used for $Oh = 1$ to identify it more easily.

numbers Re_δ, C_d converges asymptotically towards a Re_δ^{-1} scaling, consistent with the capillary-viscous scaling of the contraction velocity $U_\sigma = \sigma/\mu_l$.

As the Re_δ increases, C_d deviates from that scaling and becomes more flat. The drag coefficients at the maximum contraction velocity (empty diamonds) converge towards an asymptotic value around 1.3. However, C_d decreases systematically after this peak, and the C_d does not collapse onto a master curve depending only on Re_δ. This evolution of C_d clearly illustrates the deviation of the contraction velocity from the constant drag coefficient theory $U^* = Ct^{*-0.2}$ discussed in § 3.3. If we consider the case of $Oh = 0.1$, the aspect ratio is nearly constant before the oscillations as shown in figure 10(*b*). This deviation from the constant drag coefficient theory can therefore not be explained by this simple characterisation of the rim geometry. A more detailed analysis of the drag force around an air cylinder would be needed to better explain the scaling $U^* \sim t^{*-0.15}$ observed at low Oh. The curvature along the interface of the rim probably plays an important role, which cannot be captured by a simple aspect ratio measurement.

4.3. *Transitions between the contraction regimes*

We observed that the contraction dynamics regime of an air sheet depends on the global Ohnesorge number Oh, but also evolves in time with the local geometry of the rim. The relevant parameter to characterise the contraction dynamics of an air sheet is therefore its local Ohnesorge number Oh_δ based on the local time evolving thickness

https://doi.org/10.1017/jfm.2020.385 Published online by Cambridge University Press

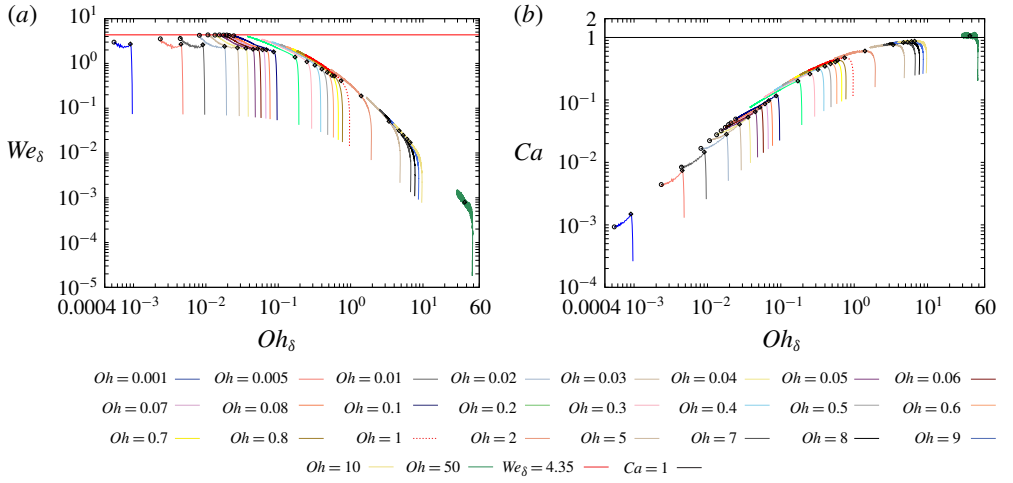


FIGURE 12. (*a*) Local Weber number We_δ, versus the local Ohnesorge number Oh_δ in log–log scale for different Ohnesorge numbers, and (*b*) capillary number Ca, versus the local Ohnesorge number Oh_δ in log–log scale for different Ohnesorge numbers. The constants $We_\delta = 4.35$ and $Ca = 1$ are plotted in panels (*a*) and (*b*), respectively, for comparison. The local Weber number We_δ and local capillary number Ca corresponding to the maximum contraction velocity are indicated by empty diamond, the local Weber number We_δ and local capillary number Ca corresponding to the starting time of the oscillations are indicated by empty circle and the data after oscillation are not plotted for $Oh \leqslant 0.1$. A dashed line is used for $Oh = 1$ for clarity.

of the rim. At low local Oh_δ, viscous effects can be neglected compared to inertia, and the dynamics can therefore be characterised by a local Weber number We_δ,

$$We_\delta = \frac{\rho_l U^2 \delta}{\sigma}.$$

In contrast, at large Oh_δ inertia can be neglected compared to viscous effects, leading to the dynamics controlled by a local capillary number Ca,

$$Ca = \frac{\mu_l U}{\sigma}.$$

This transition between the two asymptotic regimes during the contraction is clearly illustrated in figure 12, showing the time evolution of the local We_δ and Ca as a function of the Oh_δ. It corresponds to the local equivalent of figure 3(*b*) including the complete time evolution of the contraction dynamics.

The local Weber number We_δ corresponds to the square of the contraction velocity non-dimensionalised by a capillary-inertial velocity based on the local rim thickness δ rather than the film thickness e, as presented in figure 2. According to the theory presented in § 3.3, We_δ should be constant in the capillary-inertial regime (see (3.6)). This corresponds also to the constant drag coefficient at large Re_δ discussed previously, considering that $We_\delta = 4/C_d$ with the definition used in figure 11. However, the We_δ still evolves in time for all air film contractions in the low viscosity regime. This time evolution in the smooth contraction regime reaches a consistent maximum of $We_\delta =$

https://doi.org/10.1017/jfm.2020.385 Published online by Cambridge University Press

4.35 when the rim starts oscillating (see figure 12*a*). This critical local Weber number We_δ therefore characterises the transition to the oscillations of the rim. The critical Re_δ leading to the oscillations thus increases with decreasing Oh_δ, in contrast with the flow around a solid cylinder where the vortex shedding appears at a characteristic Reynolds number.

In contrast, at large Oh_δ the capillary number Ca converges towards an asymptotic value around $Ca = 1$ (see figure 12*b*). This local characterisation of the rim dynamics better illustrates this capillary viscous limit than the time evolution curves presented in figure 6, showing that the rim evolves towards lower values of Oh_δ in time.

4.4. *Oscillations of the rim*

We observed earlier that in the low Ohnesorge regime $Oh \leqslant 0.1$, some oscillations appear on the contraction velocity (figure 2), characteristic of the rim oscillations and vorticity shedding (figure 4*a*,*d*,*g*). These oscillations are qualitatively similar to the vortex induced oscillations of a flexible cylinder (Williamson & Govardhan 2004). In this section, we analyse these oscillations, and their influence on the contraction velocity. As defined in § 3.2, we formally define such oscillations as when the y-coordinate of the x-maximum point of the air sheet is larger than half of the initial sheet thickness ($|y^*_{x_{max}}| > 0.5$).

We track the three characteristic points of the rim defined in § 4.1 (also see inset of figure 13*d*): the top point, y-maximum point (x_t, y_t); the bottom point, y-minimum point (x_b, y_b); and the end point, x-maximum point $(x_{max}, y_{x_{max}})$. The time evolution of the rim geometry can be derived from these points, with a typical example shown in figure 13 for $Oh = 0.05$. We observe that the smooth oscillations of the rim geometry are well correlated with the oscillations of the contraction velocity. The difference of x-coordinates between the top and bottom point of the rim ($\Delta x^* = x^*_t - x^*_b$), and the y-coordinate of the x-maximum point of the rim $y^*_{x_{max}}$ both oscillate and show good consistence in periodicity. The contraction velocity U^* oscillates with a decreasing average $\overline{U^*}$ in time (figure 13*c*), calculated over one oscillation period. The thickness of the rim ($\delta^* = y^*_t - y^*_b$) oscillates with an increasing average $\overline{\delta^*}$ (figure 13*d*). As a result, the local Reynolds number Re_δ oscillates with an increasing average $\overline{Re_\delta}$ during the contraction (figure 13*b*).

For $0.04 \leqslant Oh \leqslant 0.1$, the oscillations of $y^*_{x_{max}}$ are quite regular (see figure 13, figure 14 and the supplementary material for the other curves). The period and amplitude of these oscillations both increase in time, as indicated by the vertical dashed lines in figure 13. These oscillations are consistent with the shedding of alternating sign vortices, forming a vortex street as observed in the insets of figure 14. The oscillations start earlier and with a higher frequency for lower Oh.

As the Oh further decreases, the oscillations become more irregular. For $Oh = 0.03$, some higher amplitude oscillations develop with a longer period, modulated by a smaller amplitude oscillation. For $Oh = 0.02$, the $y^*_{x_{max}}$ profile shows a 'double peaks' shape in a half-period of oscillation, each peak corresponding to a vortex shedding event. The rim eventually detaches from the sheet at $t^* = 862.5$. For $Oh \leqslant 0.01$, the fast deformations of the interface lead to pinch-off rapidly during the contraction, which does not show regular oscillations anymore.

We can quantify the variations of the oscillations frequency $f = 1/T$ by defining the Strouhal number as

$$St = \frac{f\delta}{U}, \tag{4.1}$$

https://doi.org/10.1017/jfm.2020.385 Published online by Cambridge University Press

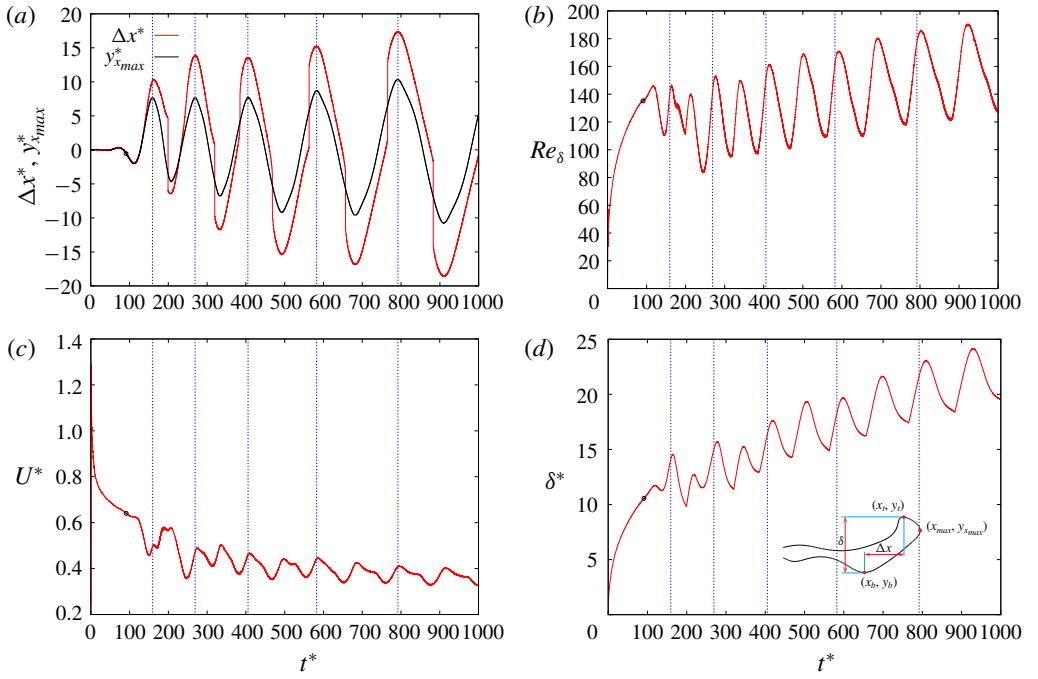


FIGURE 13. Time evolution of the oscillation of the rim at $Oh = 0.05$. (*a*) Difference of x-coordinates between the top and bottom points of the rim Δx^* versus time t^* and y-coordinate of the x-maximum point of the rim $y^*_{x_{max}}$ versus time t^*. (*b*) Local Reynolds number of the rim Re_δ versus time t^*. (*c*) Contraction velocity of the rim U^* versus time t^*. (*d*) Thickness of the rim δ^* versus time t^*, inset shows the definition of $\Delta x^* = x^*_t - x^*_b$ and $\delta^* = y^*_t - y^*_b$, the rim profile is taken from $Oh = 0.05$ at $t^* = 175$. Vertical dashed lines indicate the reference time used to measure the oscillations period. The starting time of the oscillations is indicated by an empty circle. Here, $x^* = x/e$, $y^* = y/e$, $U^* = U/U_\rho$ and $t^* = t/\tau_\rho$.

where δ is the rim thickness and U the contraction velocity. We estimate the oscillation period T by taking the time difference between each positive peak of $y^*_{x_{max}}$, indicated as filled circles in figure 14. Only the large amplitude oscillations across the centre line of the film are considered by taking only the first positive peak of $y^*_{x_{max}}$. Since the thickness of the rim and the contraction velocity oscillate in time, we take the average value of δ/U in a period T to calculate an average Strouhal number $\overline{St}$.

As shown in figure 15(*a*), the average Strouhal number $\overline{St}$ of these oscillations stays between 0.22 and 0.25 when $0.04 \leqslant Oh \leqslant 0.1$, with a slight decrease with Oh. Lower values of $\overline{St}$ are observed for $Oh = 0.03$ and $Oh = 0.02$, characteristic of the multiple vorticity shedding events over a longer period of oscillation. The evolution of the $\overline{St}$ can be understood from the local properties of the flow around the rim, in a similar way as for the vorticity shedding behind a solid cylinder. A consistent behaviour emerges if we plot $\overline{St}$ as a function of the average local Reynolds number $\overline{Re_\delta}$ over the oscillation period in figure 15(*b*). For $\overline{Re_\delta} < 200$, $\overline{St}$ increases slightly with $\overline{Re_\delta}$, from 0.22 to 0.25. A clear transition is observed at $\overline{Re_\delta} \approx 200$. For $\overline{Re_\delta} > 200$, the average Strouhal number $\overline{St}$ decreases with $\overline{Re_\delta}$, corresponding to a more complex vorticity shedding.

https://doi.org/10.1017/jfm.2020.385 Published online by Cambridge University Press

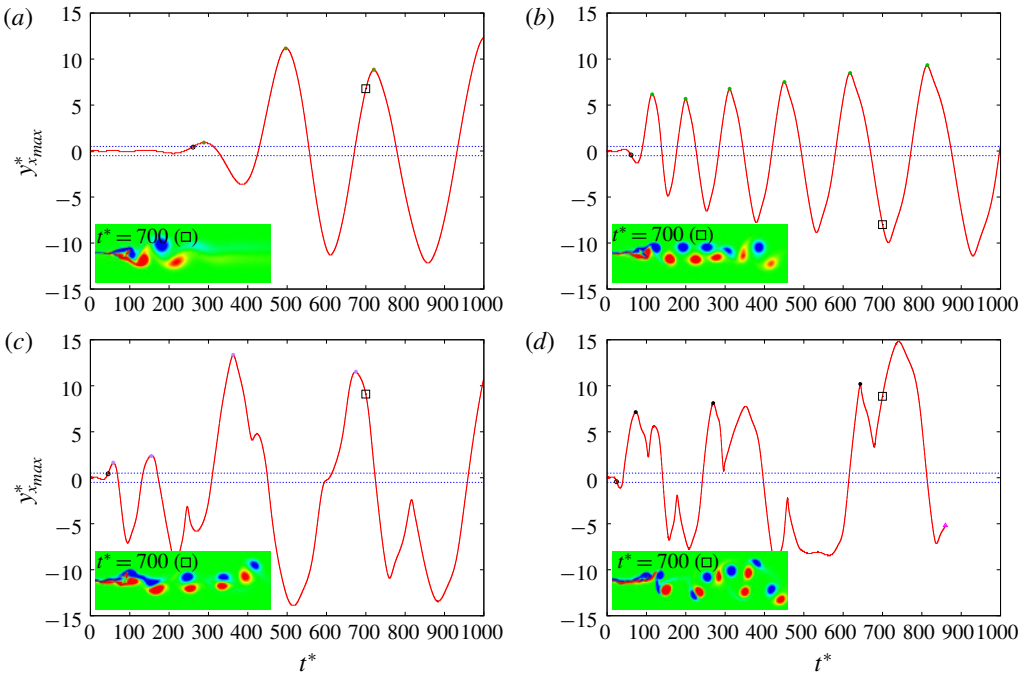


FIGURE 14. The y-coordinate of the x-maximum point of the rim $y^*_{x_{max}}$ versus time t^* at (*a*) $Oh = 0.1$, (*b*) $Oh = 0.04$, (*c*) $Oh = 0.03$ and (*d*) $Oh = 0.02$. Insets show the vorticity contour at $t^* = 700$ (indicated by an empty square on the curve). Horizontal dashed lines indicate the threshold of oscillation $y^* = 0.5$ and $y^* = -0.5$. Filled circles indicate the boundaries of a period used to calculate the average Strouhal number $\overline{St}$ and different colour is used for different Ohnesorge number as in figure 15. The starting time of the oscillations is indicated by an empty circle. The data after pinch-off are not plotted for $Oh = 0.02$, with the pinch-off time indicated by an empty triangle at $t^* = 862.5$. Here, $y^* = y/e$ and $t^* = t/\tau_\rho$ (see supplementary material for additional figures with Ohnesorge numbers from $Oh = 0.02$ to $Oh = 0.2$).

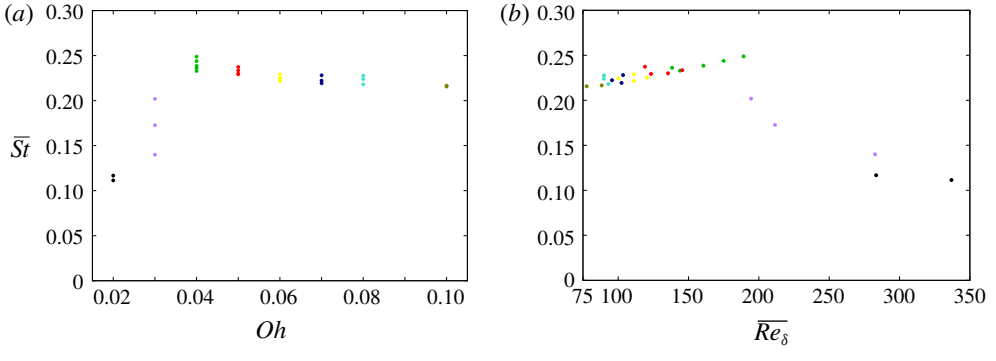


FIGURE 15. Average Strouhal number $\overline{St}$ versus Ohnesorge number Oh (*a*) and versus the average local Reynolds number $\overline{Re_\delta}$ (*b*) for $0.02 \leqslant Oh \leqslant 0.1$. Different colours are used for the different Ohnesorge numbers.

https://doi.org/10.1017/jfm.2020.385 Published online by Cambridge University Press

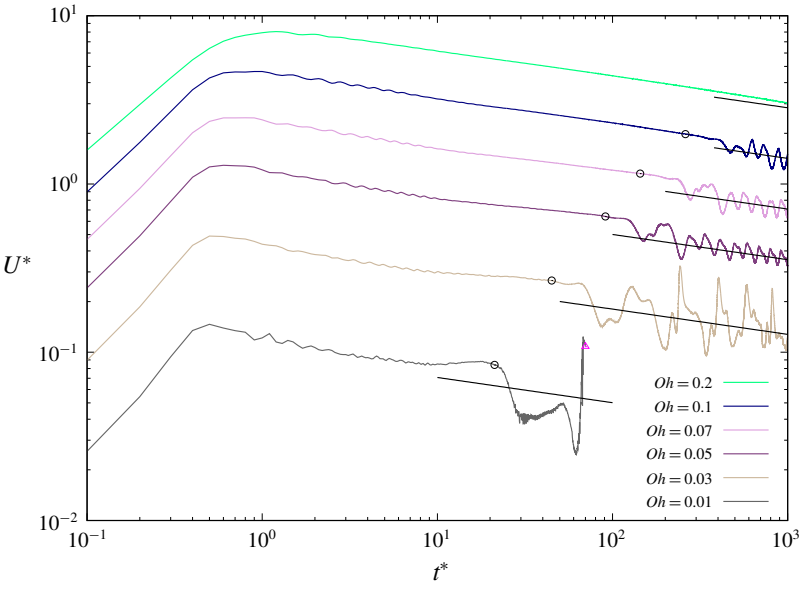


FIGURE 16. Average contraction velocity of the oscillation regime for different Ohnesorge numbers in log–log scale. The vertical position of the curve for $Oh = 0.05$ corresponds to the vertical axis values and the other curves are shifted vertically for clear view. The same scaling law of the contraction velocity $U^* = t^{*-0.15}$ (black line) is plotted in the oscillation part for all the Ohnesorge numbers. The starting time of the oscillations is indicated by an empty circle. The data after pinch-off are not plotted for $Oh = 0.01$, with the pinch-off time indicated by an empty triangle at $t^* = 72.5$. The non-oscillating case $Oh = 0.2$ is plotted for comparison. Here, $U^* = U/U_\rho$ and $t^* = t/\tau_\rho$.

The influence of these oscillations on the contraction velocity is shown in figure 16. As expected, the mean contraction velocity decreases when the rim enters into the oscillations regime, due to the increased added mass and viscous dissipation. However, it still follows the same scaling $U^* \sim t^{*-0.15}$ on average.

5. Conclusion

We have investigated the contraction of a two-dimensional air sheet in a surrounding liquid by solving the two-dimensional two-phase Navier–Stokes equations. We have confirmed that in a large range of Ohnesorge numbers, the contraction dynamics follow a similar trend, with an initial increase to a maximum velocity before decreasing. The maximum contraction velocity converges towards a capillary-inertial velocity at low Oh and a capillary-viscous velocity at high Oh. We have identified three different regimes of the contraction dynamics, in a similar way as for the contraction of a liquid film. At low Oh ($Oh \leqslant 0.1$), the contracting rim sheds vortices of alternating signs and some capillary waves propagate ahead of the rim. The deformations induced can eventually lead to the pinch-off of bubbles at the lowest Oh ($Oh \leqslant 0.02$). At intermediate Oh ($0.1 < Oh \leqslant 1$), the contraction of a rounded rim is stabilised by viscosity. At larger Oh, the rim becomes more elongated with a viscosity limited contraction velocity.

We found that the asymptotic contraction velocity follows a scaling $U \sim t^{-0.15}$ that is different from the scaling $t^{-0.2}$ deduced under the assumption of a constant drag

https://doi.org/10.1017/jfm.2020.385 Published online by Cambridge University Press

coefficient. We explained the fundamental differences between the contraction of a liquid film and an air film by the increased ratio of energy dissipated by viscous effects.

The dynamics of an air sheet can be understood by the local properties of the flow. The transition between the capillary-viscous and capillary-inertial regimes is a time evolving process characterised by the local Ohnesorge number Oh_δ. The analogy with a solid cylinder shows similar scalings of the drag coefficient and oscillation frequency. However, the transition to oscillations is characterised for the contraction of an air sheet by a critical local Weber number We_δ.

An air sheet contracting in a surrounding liquid will eventually break up due to three-dimensional instabilities (Thoroddsen *et al.* 2012) relevant for the formation of microbubbles in turbulent breaking waves (Chan *et al.* 2018, 2019). Further three-dimensional simulations and modelling are therefore needed to understand these instabilities and investigate their effect on the dynamics of the rupturing front. It will be interesting, especially, to understand if the vorticity shedding and vertical oscillations predicted in 2-D simulations at low *Oh* can be observed experimentally, as for the vortex street observed below an impacting drop (Castrejón-Pita *et al.* 2012; Thoraval *et al.* 2012, 2013), or if the 3-D instabilities prevent their coherent formation. These oscillations could provide a theoretical 2-D path to the rupture of air films, but may never be observed experimentally due to 3-D effects.

Acknowledgements

Z.J. acknowledges the financial support from the National Natural Science Foundation of China (grant no. 11802226). P.D. and M.-J.T. acknowledge the helpful discussions with A. Berny and T. Séon. M.-J.T. acknowledges the financial support from the National Natural Science Foundation of China (grant nos. 11542016, 11702210 and 11850410439) and the Project B18040. M.-J.T. is also supported by the Cyrus Tang Foundation through the Tang Scholar program.

Declaration of interests

The authors report no conflict of interest.

Supplementary material and movies

Supplementary material and movies are available at https://doi.org/10.1017/jfm.2020.385.

REFERENCES

Beilharz, D., Guyon, A., Li, E. Q., Thoraval, M.-J. & Thoroddsen, S. T. 2015 Antibubbles and fine cylindrical sheets of air. *J. Fluid Mech.* **779**, 87–115.

Brenner, M. P. & Gueyffier, D. 1999 On the bursting of viscous films. *Phys. Fluids* **11** (3), 737–739.

Castrejón-Pita, A. A., Castrejón-Pita, J. R. & Hutchings, I. M. 2012 Experimental observation of von Kármán vortices during drop impact. *Phys. Rev.* E **86** (4), 045301(R).

Chan, W. H. R., Mirjalili, S., Jain, S. S., Urzay, J., Mani, A. & Moin, P. 2018 Video: Birth of microbubbles in turbulent breaking waves. In *71th Annual Meeting of the APS Division of Fluid Dynamics – Gallery of Fluid Motion,* V0027. American Physical Society.

Chan, W. H. R., Mirjalili, S., Jain, S. S., Urzay, J., Mani, A. & Moin, P. 2019 Birth of microbubbles in turbulent breaking waves. *Phys. Rev. Fluids* **4** (10), 100508.

https://doi.org/10.1017/jfm.2020.385 Published online by Cambridge University Press

CHEBIL, M. S., MCGRAW, J. D., SALEZ, T., SOLLOGOUB, C. & MIQUELARD-GARNIER, G. 2018 Influence of outer-layer finite-size effects on the dewetting dynamics of a thin polymer film embedded in an immiscible matrix. *Soft Matt.* **14** (30), 6256–6263.

CULICK, F. E. C. 1960 Comments on a Ruptured Soap Film. *J. Appl. Phys.* **31** (6), 1128–1129.

CZERSKI, H., TWARDOWSKI, M., ZHANG, X. & VAGLE, S. 2011 Resolving size distributions of bubbles with radii less than 30 μm with optical and acoustical methods. *J. Geophys. Res.* **116**, C00H11.

DEBRÉGEAS, G., DE GENNES, P.-G. & BROCHARD-WYART, F. 1998 The life and death of "bare" viscous bubbles. *Science* **279** (5357), 1704–1707.

DEBRÉGEAS, G., MARTIN, P. & BROCHARD-WYART, F. 1995 Viscous bursting of suspended films. *Phys. Rev. Lett.* **75** (21), 3886–3889.

DEIKE, L., MELVILLE, W. K. & POPINET, S. 2016 Air entrainment and bubble statistics in breaking waves. *J. Fluid Mech.* **801**, 91–129.

DERBY, B. 2010 Inkjet printing of functional and structural materials: fluid property requirements, feature stability, and resolution. *Annu. Rev. Mater. Res.* **40**, 395–414.

DORBOLO, S., CAPS, H. & VANDEWALLE, N. 2003 Fluid instabilities in the birth and death of antibubbles. *New J. Phys.* **5**, 161.

DORBOLO, S., REYSSAT, E., VANDEWALLE, N. & QUÉRÉ, D. 2005 Aging of an antibubble. *Eur. Phys. Lett.* **69** (6), 966–970.

DORBOLO, S., TERWAGNE, D., DELHALLE, R., DUJARDIN, J., HUET, N., VANDEWALLE, N. & DENKOV, N. 2010 Antibubble lifetime: influence of the bulk viscosity and of the surface modulus of the mixture. *Colloids Surf.* A **365** (1–3), 43–45.

EGGERS, J., LISTER, J. R. & STONE, H. A. 1999 Coalescence of liquid drops. *J. Fluid Mech.* **401**, 293–310.

ESMAILIZADEH, L. & MESLER, R. 1986 Bubble entrainment with drops. *J. Colloid Interface Sci.* **110** (2), 561–574.

DE GENNES, P.-G., BROCHARD-WYART, F. & QUÉRÉ, D. 2004 *Capillarity and Wetting Phenomena: Drops, Bubbles, Pearls, Waves*. Springer.

GORDILLO, L., AGBAGLAH, G., DUCHEMIN, L. & JOSSERAND, C. 2011 Asymptotic behavior of a retracting two-dimensional fluid sheet. *Phys. Fluids* **23** (12), 122101.

HICKS, P. D. & PURVIS, R. 2011 Air cushioning in droplet impacts with liquid layers and other droplets. *Phys. Fluids* **23** (6), 062104.

JIAN, Z., CHANNA, M. A., KHERBECHE, A., CHIZARI, H., THORODDSEN, S. T. & THORAVAL, M.-J. 2020 To split or not to split: dynamics of an air disk formed under a drop impacting on a pool. *Phys. Rev. Lett.* **124** (18), 184501.

JOSSERAND, C., RAY, P. & ZALESKI, S. 2016 Droplet impact on a thin liquid film: anatomy of the splash. *J. Fluid Mech.* **802**, 775–805.

JOSSERAND, C. & THORODDSEN, S. T. 2016 Drop impact on a solid surface. *Annu. Rev. Fluid Mech.* **48**, 365–391.

KIGER, K. T. & DUNCAN, J. H. 2012 Air-entrainment mechanisms in plunging jets and breaking waves. *Annu. Rev. Fluid Mech.* **44**, 563–596.

LANGLEY, K. R. & THORODDSEN, S. T. 2019 Gliding on a layer of air: impact of a large-viscosity drop on a liquid film. *J. Fluid Mech.* **878**, R2.

LEGENDRE, D., LAUGA, E. & MAGNAUDET, J. 2009 Influence of slip on the dynamics of two-dimensional wakes. *J. Fluid Mech.* **633**, 437–447.

MILLS, B. H., SAYLOR, J. R. & TESTIK, F. Y. 2012 An experimental study of Mesler entrainment on a surfactant-covered interface: the effect of drop shape and Weber number. *AIChE J.* **58** (1), 46–58.

MIRJALILI, S., CHAN, W. H. R. & MANI, A. 2018 High Fidelity simulations of micro-bubble shedding from retracting thin gas films in the context of liquid–liquid impact. In *32nd Symposium on Naval Hydrodynamics, Hamburg, Germany*, arXiv:1811.12352.

OGUZ, H. N. & PROSPERETTI, A. 1989 Surface-tension effects in the contact of liquid surfaces. *J. Fluid Mech.* **203**, 149–171.

https://doi.org/10.1017/jfm.2020.385 Published online by Cambridge University Press

PANDIT, A. B. & DAVIDSON, J. F. 1990 Hydrodynamics of the rupture of thin liquid films. *J. Fluid Mech.* **212**, 11–24.

POPINET, S. 2019 Basilisk. http://basilisk.fr.

REYSSAT, É. & QUÉRÉ, D. 2006 Bursting of a fluid film in a viscous environment. *Eur. Phys. Lett.* **76** (2), 236–242.

SAVVA, N. & BUSH, J. W. M. 2009 Viscous sheet retraction. *J. Fluid Mech.* **626**, 211–240.

SAYLOR, J. R. & BOUNDS, G. D. 2012 Experimental study of the role of the Weber and capillary numbers on Mesler entrainment. *AIChE J.* **58** (12), 3841–3851.

SCHEID, B., DORBOLO, S., ARRIAGA, L. R. & RIO, E. 2012 Antibubble dynamics: the drainage of an air film with viscous interfaces. *Phys. Rev. Lett.* **109** (26), 264502.

SCHEID, B., ZAWALA, J. & DORBOLO, S. 2014 Gas dissolution in antibubble dynamics. *Soft Matt.* **10** (36), 7096–7102.

SIGLER, J. & MESLER, R. 1990 The behavior of the gas film formed upon drop impact with a liquid surface. *J. Colloid Interface Sci.* **134** (2), 459–474.

SOB'YANIN, D. N. 2015 Theory of the antibubble collapse. *Phys. Rev. Lett.* **114** (10), 104501.

SONG, M. & TRYGGVASON, G. 1999 The formation of thick borders on an initially stationary fluid sheet. *Phys. Fluids* **11** (9), 2487–2493.

SÜNDERHAUF, G., RASZILLIER, H. & DURST, F. 2002 The retraction of the edge of a planar liquid sheet. *Phys. Fluids* **14** (1), 198–208.

TAYLOR, G. 1959 The dynamics of thin sheets of fluid. II. Waves on fluid sheets. *Proc. R. Soc. Lond.* A **253** (1274), 296–312.

THORAVAL, M.-J., TAKEHARA, K., ETOH, T. G., POPINET, S., RAY, P., JOSSERAND, C., ZALESKI, S. & THORODDSEN, S. T. 2012 von Kármán vortex street within an impacting drop. *Phys. Rev. Lett.* **108** (26), 264506.

THORAVAL, M.-J., TAKEHARA, K., ETOH, T. G. & THORODDSEN, S. T. 2013 Drop impact entrapment of bubble rings. *J. Fluid Mech.* **724**, 234–258.

THORAVAL, M.-J. & THORODDSEN, S. T. 2013 Contraction of an air disk caught between two different liquids. *Phys. Rev.* E **88** (6), 061001(R).

THORODDSEN, S. T., ETOH, T. G. & TAKEHARA, K. 2003 Air entrapment under an impacting drop. *J. Fluid Mech.* **478**, 125–134.

THORODDSEN, S. T., ETOH, T. G., TAKEHARA, K., OOTSUKA, N. & HATSUKI, Y. 2005 The air bubble entrapped under a drop impacting on a solid surface. *J. Fluid Mech.* **545**, 203–212.

THORODDSEN, S. T., THORAVAL, M.-J., TAKEHARA, K. & ETOH, T. G. 2012 Micro-bubble morphologies following drop impacts onto a pool surface. *J. Fluid Mech.* **708**, 469–479.

TOMIYAMA, A., KATAOKA, I., ZUN, I. & SAKAGUCHI, T. 1998 Drag coefficients of single bubbles under normal and micro gravity conditions. *JSME Intl J.* B **41** (2), 472–479.

TRAN, T., DE MALEPRADE, H., SUN, C. & LOHSE, D. 2013 Air entrainment during impact of droplets on liquid surfaces. *J. Fluid Mech.* **726**, R3.

VANDEWALLE, N., TERWAGNE, D., GILET, T., CAPS, H. & DORBOLO, S. 2009 Antibubbles, liquid onions and bouncing droplets. *Colloids Surf.* A **344** (1–3), 42–47.

WANNINKHOF, R., ASHER, W. E., HO, D. T., SWEENEY, C. & MCGILLIS, W. R. 2009 Advances in quantifying air–sea gas exchange and environmental forcing. *Annu. Rev. Marine Sci.* **1**, 213–244.

WILLIAMSON, C. H. K. & GOVARDHAN, R. 2004 Vortex-induced vibrations. *Annu. Rev. Fluid Mech.* **36**, 413–455.

YAN, X., JIA, Y., WANG, L. & CAO, Y. 2017 Drag coefficient fluctuation prediction of a single bubble rising in water. *Chem. Engng J.* **316**, 553–562.

YARIN, A. L. 2006 Drop impact dynamics: splashing, spreading, receding, bouncing... *Annu. Rev. Fluid Mech.* **38**, 159–192.

ZOU, J., JI, C., YUAN, B., RUAN, X. & FU, X. 2013 Collapse of an antibubble. *Phys. Rev.* E **87** (6), 061002(R).

https://doi.org/10.1017/jfm.2020.385 Published online by Cambridge University Press